Separation and Purification Technology 303 (2022) 122212

Contents lists available at ScienceDirect

Separation and Purification Technology

journal homepage: www.elsevier.com/locate/seppur

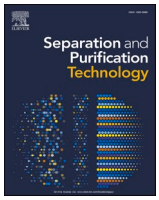

Separatable MoS_2 loaded biochar/$CaCO_3$/Alginate gel beads for selective and efficient removal of Pb(II) from aqueous solution

Yingnan He [a], Xiuxiu Jia [a], Shuxing Zhou [b,*], Jianbing Chen [c], Shusheng Zhang [d], Xiaohua Li [e], Yimin Huang [a,*], Thomas Wågberg [f], Guangzhi Hu [a,f,*]

[a] Institute for Ecological Research and Pollution Control of Plateau Lakes, School of Ecology and Environmental Science, Yunnan University, Kunming 650504, China
[b] Hubei Key Laboratory of Low Dimensional Optoelectronic Materials and Devices, Hubei University of Arts and Science, Xiangyang 441053, China
[c] Research Academy of Non-metallic Mining Industry Development, Materials and Environmental Engineering College, Chizhou University, Chizhou 247000, China
[d] College of Chemistry, Zhengzhou University, Zhengzhou 450000, China
[e] Rural Energy & Environment Agency, Ministry of Agriculture and Rural Affairs, Beijing 100125, China
[f] Department of Physics, Umeå University, S-901 87 Umeå, Sweden

ARTICLE INFO

Keywords:
Sodium alginate gel beads
Biochar
High capacity
Lead removal
Room temperature adsorption

ABSTRACT

Centimeter-scale composite biochar-alginate gel beads ($MoS_2B/CaCO_3/Alg$) were designed for the adsorption of Pb(II) in water using MoS_2 modified biochar as the filler, alginate as the matrix, and $CaCO_3$ as the active additive component. The composite gel beads were characterized using scanning electron microscope (SEM), X-ray photoelectron spectroscopy (XPS), Fourier transform infrared (FTIR), X-ray diffraction (XRD), and other techniques. $MoS_2B/CaCO_3/Alg$ showed excellent adsorption capacity over a wide range of pH 4–7. The maximum adsorption capacities obtained using the Langmuir model were 769.2, 833.3, and 909.1 mg g^{-1} at 10, 25 and 40 °C, respectively. At a dosing rate of 0.4 g L^{-1}, $MoS_2B/CaCO_3/Alg$ was able to reduce the Pb(II) concentration to below 0.05 ppm in complex simulated lead battery wastewater. After 10 repeated cycles, $MoS_2B/CaCO_3/Alg$ maintained a high removal rate of 98.4 %. This spherical adsorbent is simple to prepare and easy to recover, has an ultra-high adsorption capacity, and is mechanically stable and resistant to interference, thus it is expected to be suitable for application in industrial wastewater treatment.

1. Introduction

Lead is the largest non-radioactive element in terms of atomic weight and has a low melting point, high corrosion resistance and good plasticity, making it suitable for wide use in industry [1]. Current lead-containing wastewater mainly comes from the battery, electroplating and non-ferrous metal mining and smelting industries, and most of the lead element in industrial wastewater exists in the form of Pb(II). Lead enters the human body through the digestive and respiratory tracts, and its excessive deposition in the human body can substantially impair the normal development and functioning of the nervous and cardiovascular systems, two of the major body systems [2], and these negative effects are particularly more severe for children. Therefore, it is important to reduce the concentration of Pb(II) in industrial effluents to a safe level. Adsorption is currently regarded as a well-established and inexpensive method for removing heavy metal ions, in which selection of an efficient and economical adsorbent is crucial.

Hydrogels, as newly developed polymeric material with a three-dimensional network structure, can be both hydrophilic and hydrophobic, absorbing and retaining part of the water in aqueous solutions but not dissolving themselves [3]. Natural polysaccharide hydrogels are sourced from natural and microbial resources, are inexpensive, and can be broken down by microorganisms into water, carbon dioxide, and inorganic small molecules following disposal without the formation of any secondary contamination [4]. Sodium alginate, a linear hydroxyl-rich natural anionic polysaccharide can form a hydrogel network with most of the divalent metal ions [5,6]. Alginate hydrogels have received much attention in the field of adsorption in recent years and contain abundant macro and mesoporous structures which can be designed into desirable shapes and sizes [7,8]. However, the poor mechanical strength of alginate hydrogels and their highly pH-dependent adsorption process limit their practical applicability [9]. By introducing inorganic or organic fillers (graphene oxide [10], biochar [11], metals and metal oxides [12], clay minerals [13], silica-based materials [14], etc.) into the

* Corresponding authors.
E-mail addresses: sxzhou@hbuas.edu.cn (S. Zhou), huangyimin@ynu.edu.cn (Y. Huang), guangzhi.hu@umu.se (G. Hu).

https://doi.org/10.1016/j.seppur.2022.122212
Received 7 August 2022; Received in revised form 15 September 2022; Accepted 21 September 2022
Available online 27 September 2022

hydrogel system, its physical and chemical properties can be modified enhancing the adsorption properties as well as the mechanical strength, while also solving the problem of the difficult recovery of nanomaterials. MoS_2 nanomaterials contain abundant active S-functional groups and exhibit strong affinity for metal ions. It is currently considered to be a promising adsorbent and has been used to adsorb arsenic [15], chromium [16], and cadmium [17] in water. However, pure nano-MoS_2 particles have low dispersibility in solution and tend to aggregate, and its S atoms are difficult to expose and combine with heavy metal ions. As one of the world's recognized harmful invasive plants, water hyacinth is rich in cellulose, hemicellulose and nitrogen. Water hyacinth can form self-doped nitrogen porous biochar after pyrolysis, which provides a large specific surface area and the ability to act as an electron shuttle and electron donor [18], and is an excellent carrier for supporting MoS_2 nanoparticles.

In this study, MoS_2 nanosheets were incorporated on the surface of biochar using a hydrothermal one-pot synthesis method to form a cluster structure. Owing to the presence of sulfur, MoS_2 has an excellent affinity for metal ions and therefore, improves the adsorption capacity [19]. The introduction of MoS_2-modified biochar into the alginate mechanism, using the coupling between components contributed to the formation of the gel network and enhanced adsorption performance. We found that the dense particle structure after the addition of biochar slowed down the diffusion process of heavy metal ions in the gel beads, and the adsorption rate was slow. To address this issue, $CaCO_3$ was used as a porogenic agent to create pore-like structures within the hydrogel, which enhances the adsorption rate, while the residual $CaCO_3$ can act as a pH buffer to expand the available pH range for the adsorption process. Residual $CaCO_3$ can also act as an active ingredient for Pb(II) adsorption.

$MoS_2B/CaCO_3$/Alg gel beads were synthesized using MoS_2 modified biochar as a filler, alginate as a carrier and $CaCO_3$ as a porogenic agent and active ingredient. The adsorbent has a "core-shell" bead structure, which eliminates the problem of the super-micron size of the adsorbent material and the difficulty of separation and recovery. Various characterizations of the $MoS_2B/CaCO_3$/Alg gel beads were carried out to investigate the adsorption mechanism. The effects of pH, adsorption kinetics, adsorption isotherms, adsorption thermodynamics and recoverability as well as the effect of Pb(II) adsorption on simulated real lead battery wastewater were investigated.

2. Experiment method

The materials and characterization methods used for the experiments conducted are described in the Supplementary information (**SI**).

2.1. Preparation of MoS_2/biochar

Details of all experimental reagents are provided in the **SI**. Water hyacinth was washed with alternating ethanol and water, dried, and powdered. The temperature was raised to 500 °C using a tube furnace at a heating rate of 10 °C min^{-1} and held for 2 h. The obtained biochar was washed with 1 M HCl to remove excess ash. After washing with deionized water to neutral pH, it was filtered and dried to obtain the biochar.

For the hydrothermal reaction, 1 g of biochar of anemone, 1.24 g of ammonium molybdate tetrahydrate, and 1.07 g of thiourea were poured into 60 mL of water; the solution was stirred for 30 min and the hydrothermal reaction was carried out at 180 °C for 6 h. After cooling to room temperature, the powder was filtered, washed with deionized water, and dried to obtain MoS_2B.

2.2. Preparation of porous $MoS_2B/CaCO_3$/Alg gel beads

First, 0.45 g (3 %, w/v) of sodium alginate and $CaCO_3$ were dissolved in 15 mL of water, stirred well, and MoS_2B powder was added to it and again stirred for 24 h. Then, a 3 % (w/v) $CaCl_2$ solution was added to form gel beads and left overnight. The gel beads were transferred to 400 mL of 0.05 M HCl, soaked for 3 h, and then filtered and washed to neutral using deionized water. After freezing for 30 min, the samples were freeze-dried for 12 h to obtain the porous $MoS_2B/CaCO_3$/Alg gel beads. Of which 0–3% (w/v) for $CaCO_3$ and 0–2 % (w/v) for MoS_2B powder.

2.3. Batch adsorption tests

The adsorption behavior of the porous $MoS_2B/CaCO_3$/Alg gel beads was investigated through a series of adsorption tests including the proportion of adsorbent filler, solution pH, adsorption time, temperature, competing ions, simulated wastewater, and number of cycles. Typical adsorption tests were conducted by adding a solid-to-liquid ratio of 0.2 g L^{-1} of $MoS_2B/CaCO_3$/Alg to the Pb(II) solution and shaking for 24 h. The shaker speed was 150 rpm and all tests were repeated three times.

The effects of initial pH on Pb(II) adsorption were first investigated. The effects of the addition of MoS_2/biochar and $CaCO_3$ on the adsorption of Pb(II) were carried out at pH 4. The adsorption isotherms were measured at 10, 25, and 40 °C, and the initial concentrations of Pb(II) varied between 200 and 1,000 ppb. $MoS_2B/CaCO_3$/Alg with a solid-to-liquid ratio of 0.2–1.2 g L^{-1} was added to simulated lead battery wastewater with a complex composition containing other metal ions at pH 4. A binary solution of Pb(II)/Co(II), Pb(II)/Ni(II), Pb(II)/Cd(II), Pb(II)/Cu(II) with a concentration of 100 ppm of both the metal ions was also adjusted to investigate the effect of competing ions on the adsorption of Pb(II) by $MoS_2B/CaCO_3$/Alg. The adsorption–desorption experiments of $MoS_2B/CaCO_3$/Alg were carried out at 100 ppm Pb(II). The adsorption and desorption experiments were performed 10 times consecutively. The adsorbed gel beads were filtered and shaken with 40 mL of 0.1 M HCl solution for 1 h. Pb(II) was washed from the gel spheres and the surface was rinsed with distilled water until neutral and then used again. The concentration of Pb(II) was determined by Inductively coupled plasma–optical emission spectrometry (ICP–OES) for all experiments, and the equilibrium adsorption capacity Q_e (mg g^{-1}).

$$Q_e = \frac{(C_0 - C_e) \bullet V}{m} \quad (1)$$

Where, C_0 (ppm) and C_e (ppm) are the initial and equilibrium concentrations, respectively. V (L) is the volume of the initial solution and m (g) is the mass of the adsorbent.

3. Results and discussion

3.1. Characterization results of $MoS_2B/CaCO_3$/Alg

Digital and electron microscopy images of $MoS_2B/CaCO_3$/Alg are shown in Fig. 1. In Fig. 1**a and b**, it can be seen that the gel bead formed a good core–shell structure, and the 3D porous structure formed by sodium alginate was abundant inside. At the same time, some pores generated by CO_2 generated by $CaCO_3$ after encountering acid were formed. According to the BET results (Fig. 2**i**), the gel beads had mainly mesopores, with a pore size of approximately 25.9 nm. This porous structure facilitates the diffusion and adsorption of Pb(II). After adsorption, the 3D porous structure remained strong and the surface became rough with some granular material, presumably Pb(II) was adsorbed on the surface of the material.Fig. 1**g** show a MoS_2-modified water hyacinth biochar, demonstrating the morphology of a flower-like nanostructure composed of irregular nanosheets of MoS_2 deposited on biochar.

The XPS spectral of $MoS_2B/CaCO_3$/Alg before and after adsorption are shown in Fig. 2. The C 1 s spectrum of $MoS_2B/CaCO_3$/Alg beads (Fig. 2**b**) can be divided into four major peaks, 283.98, 288.99, 285.73, 291.58 eV, corresponding to C—C/C═C, C—O, –COOH and CO_3^{2-} [20,21], respectively. After adsorption of Pb(II), –COOH and CO_3^{2-} are shifted back to 285.34, 289.16 eV. The O 1 s pattern (Fig. 2**d**) was still deconvoluted and separated into three peaks at 530.60, 531.37 and

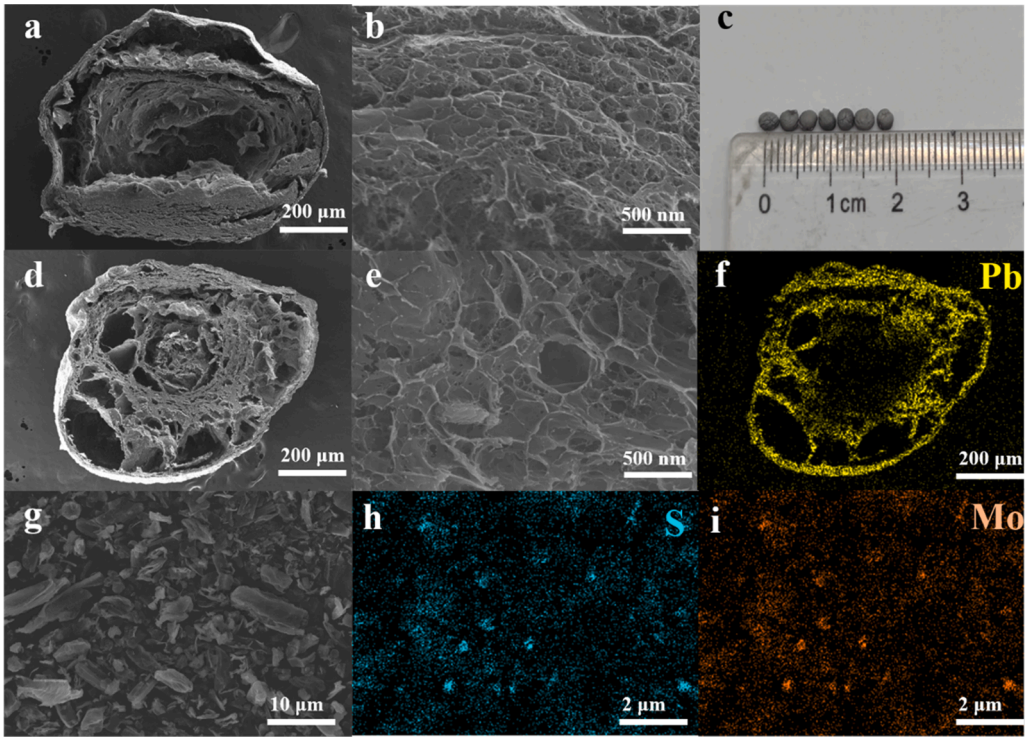

Fig. 1. Cross-sectional SEM image of $MoS_2B/CaCO_3$/Alg and after adsorption **(a, d),** internal porous structure of $MoS_2B/CaCO_3$/Alg before and after adsorption **(b, e),** digital photo of $MoS_2B/CaCO3$/Alg **(c),** EDS elemental mapping of $MoS_2B/CaCO_3$/Alg after adsorption **(f),** SEM image of MoS_2 modified biochar **(g),** EDS elemental mapping of MoS_2 modified biochar(**h, i**).

532.60 eV, corresponding to metal-O, CO_3^{2-}, and –OH [20,22]. After adsorption, the binding energy of –OH shifted back to 531.87 eV and that of metal-O decreased by 0.48 eV, indicating the formation of a Pb—O bond between Pb(II) and the O-containing group of the alginate (–COOH/–OH). However, the binding energy of CO_3^{2-} remained almost unchanged (531.373 and 531.382 eV), and its content did not decrease significantly (51.4 % and 49.9 %). The smaller change in binding energy after the adsorption of Pb(II) indicates that the electron rearrangement around the active site CO_3^{2-} was less variable, which favored ion exchange between Ca(II) and Pb(II) [23].

Following the adsorption of Pb(II), strong characteristic peaks representing Pb $4d_{3/2}$, Pb $4d_{5/2}$ and Pb 4f were observed at approximately 437, 414 and 140 eV (Total spectrum, Fig. 2**a**). The Pb 4f spectrum of $MoS_2B/CaCO_3$/Alg was deconvoluted into four peaks with binding energies of 137.62, 138.71, 142.51 eV. The peak at the binding energy of 138.71 eV for Pb $4f_{7/2}$ is probably due to the presence of $PbCO_3$ [24]. The peaks of Pb $4f_{5/2}$ at 143.59 eV and Pb $4f_{7/2}$ at 137.62 eV may be attributed to the presence of Pb—O [25], where Pb(II) forms a chelate with the carboxylate group.

FTIR spectroscopy was used to analyze the interactions between the functional groups of $MoS_2B/CaCO_3$/Alg before and after adsorption (Fig. 2**g**). All materials showed a broad characteristic peak at 3328–3347 cm^{-1} attributed to the stretching of O—H, which shifted significantly as the filler was added to the alginate matrix, implying the formation of hydrogen bonds during the gelation process. The absorption peaks at 1589–1609 cm^{-1} and 1414–1433 cm^{-1} originate from the asymmetric and symmetric vibrations of the ionic carboxyl groups. After the introduction of $CaCO_3$, the peaks at 710, 876 and 1426 cm^{-1} of $MoS_2B/CaCO_3$/Alg were observed to be typical in-plane bending, out-of-plane bending and asymmetric stretching of the C—O of the carbonate group, respectively, indicating the successful introduction of $CaCO_3$. The peak at 1426 cm^{-1} overlapped with the symmetric stretching of the ionic carboxyl group, making the peak wider than that of MoS_2B/Alg. Upon adsorption of Pb(II), both the asymmetric and symmetric peaks of the O-containing groups, including O—H and ionic carboxyl groups, shifted significantly to 3328, 1589, and 1414 cm^{-1}, respectively along with a change, in intensity, presumably owing to the possible complexation and electrostatic interactions between Pb(II) and the O-containing groups. In addition, $MoS_2B/CaCO_3$/Alg-Pb showed a peak representing Pb—O at 674 cm^{-1} [26]and a peak representing $PbCO_3$ at 877 cm^{-1} [27], proving that Pb(II) was adsorbed via ion exchange with Ca(II).

The crystalline phases of the mixture were analyzed by XRD of the adsorbed $MoS_2B/CaCO_3$/Alg (Fig. 2**h**). The characteristic peaks of $MoS_2B/CaCO_3$/Alg-Pb at $2\theta = 20.06°$, 24.79°, 25.49°, 36.13°, 43.47°, and 47.03° correspond to the $PbCO_3$ cubic phases (1 1 0), (1 1 1), (0 2 1), (0 2 2), (0 3 2), and (1 3 2), respectively, and the results are in agreement with the $PbCO_3$ standard cards (PDF# 70–2052). After adsorption, Pb (II) was adsorbed in $MoS_2B/CaCO_3$/Alg as carbonate ($PbCO_3$), indicating chemical precipitation as an important mechanism for the removal of Pb(II) from $MoS_2B/CaCO_3$/Alg.

3.2. *Effect of component ratios on adsorption performance*

To investigate the effects of different component ratios on the adsorption of Pb(II), the addition ratios of MoS_2B and $CaCO_3$ were varied. After the addition of a small amount of MoS_2B (0.125 %), both the adsorption capacity and the mechanical strength of the sodium alginate gel beads improved. However, the adsorption capacity tended to decrease when MoS_2B proportion increased further (0.25 %–2 %), which could be attributed to the partial blockage of the 3D macropores formed inside the sodium alginate gel beads by biochar, resulting in a decrease in the effective contact sites of the material. Therefore the optimum addition of MoS_2B was chosen as 0.125 %. Due to the low addition of MoS_2B, there is no need to worry about the leaching of MoS_2. When the solution was continuously shaken for twelve days, the leaching concentration of S element in the solution was 0.0205 ppb, and the leaching concentration of Mo element was 0.0033 ppb.

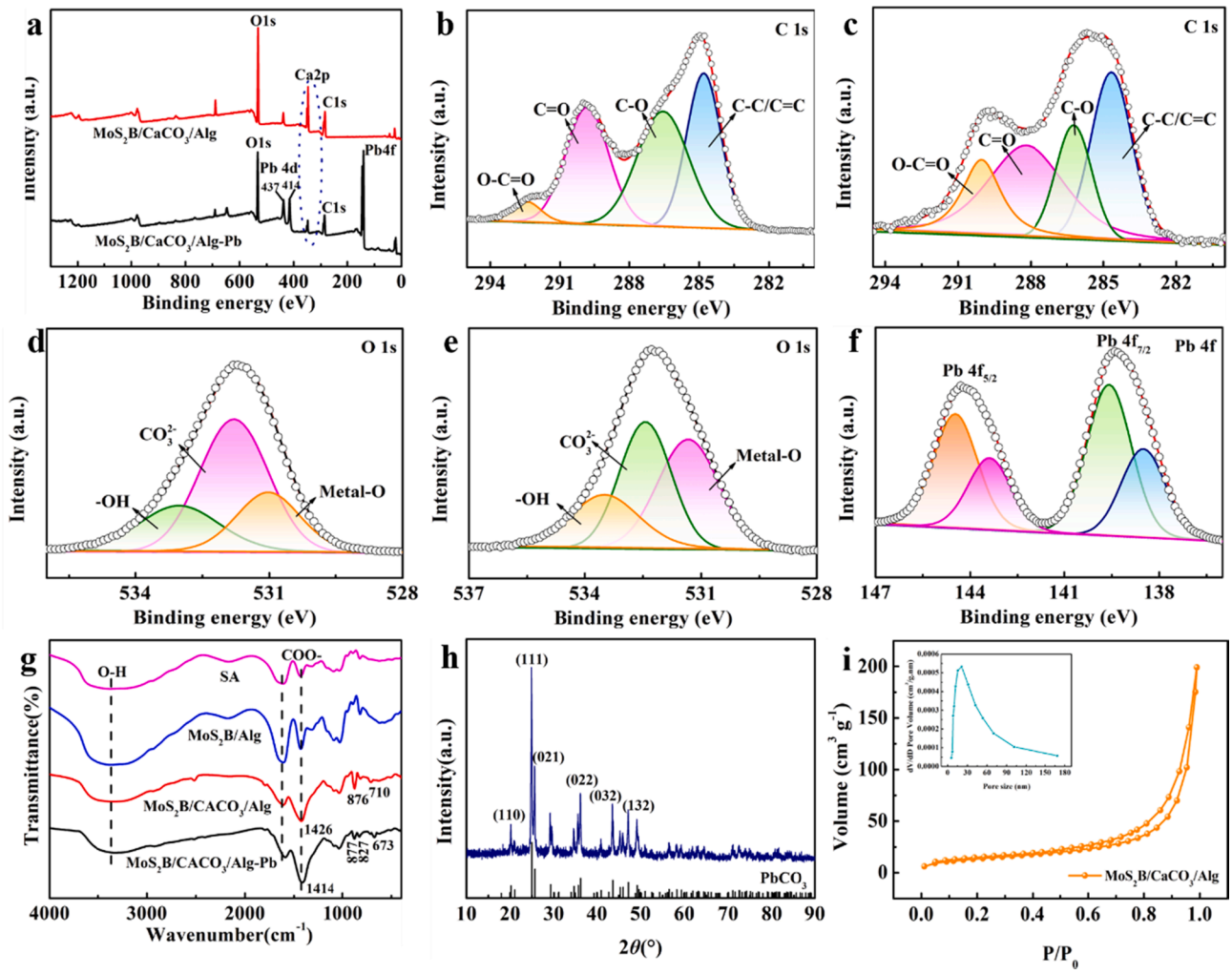

Fig. 2. XPS spectra before and after adsorption of $MoS_2B/CaCO_3/Alg$ **(a)**, C 1 s spectra of $MoS_2B/CaCO_3/Alg$ before **(b)** and after adsorption **(c)**, O 1 s spectra of $MoS_2B/CaCO_3/Alg$ before **(d)** and after adsorption **(e)**, Pb 4f spectra of $MoS_2B/CaCO_3/Alg$ after adsorption **(f)**, FTIR of $MoS_2B/CaCO_3/Alg$ before and after adsorption **(g)**, XRD pattern of $MoS_2B/CaCO_3/Alg$ after adsorption **(h)**, BET parameters of $MoS_2B/CaCO_3/Alg$ **(i)**.

By adding $CaCO_3$, the reaction of CO_3^{2-} with HCl to form CO_2 was used to create pores inside the gel beads, while generating $CaCl_2$ which also acted as a cross-linking agent for sodium alginate without introducing impurities [28]. When $CaCO_3$ was added, the adsorption of Pb(II) showed an upward trend, but at an excess of $CaCO_3$ addition, the gel solution did not easily disperse evenly and showed poor sphericity after the formation of the beads. Therefore, the optimum addition of $CaCO_3$ was chosen to be 3 % (w/v). The addition of $CaCO_3$ increased the adsorption of the gel beads by 19 % (**Fig.S4**) compared to that without the addition, which may be attributed to (1) the presence of the pore-forming properties of $CaCO_3$ that enhance the specific surface area inside the gel beads, increasing in the effective contact area for Pb(II) inside the beads, (2) The residual $CaCO_3$ inside the gel beads, which acted as a pH buffer during adsorption [29], allowed the MoS_2B/Alg gel beads to adsorb Pb(II) efficiently over a wide pH range [30].(3) Unreacted $CaCO_3$ is highly susceptible to ion exchange with Pb(II), forming $PbCO_3$ ($K_{spCaCO3} = 3.36 \times 10^{-9}$ is much larger than $K_{spPbCO3} = 7.4 \times 10^{-14}$).

By comparing the force required to generate 60 % strain of gel beads with different added components, the effects of each component on the mechanical strength of the gel beads were analyzed (**Fig.S5** for digital photos of the gel beads with different components). Alg, $CaCO_3/Alg$, MoS_2B/Alg, $MoS_2B/CaCO_3/Alg$ gel beads required 6.33, 6.18, 7.18 and 7.86 N to generate 60 % strain, respectively (Fig. 3**h**). The results show that the mechanical strength of the composite gel beads can be enhanced by adding only a small amount of modified biochar.

3.3. Solution pH and temperature effect

During adsorption, pH has a significant influence on the adsorption effect and may directly affect the surface charge of the adsorbent and the diffusion of heavy metal ions in the solution. To avoid the precipitation of Pb(II) in the solution, the effect of pH changes was investigated in the range of pH 2–7. In Fig. 3**c**, the adsorption amount of Pb(II), was only 140.8 mg g^{-1} at a pH of 2. The H^+/H_3O^+ in solution and the strong competition with Pb(II) formed [31], and the large number of carboxyl groups contained in $MoS_2B/CaCO_3/Alg$ underwent protonation at low pH, causing $MoS_2B/CaCO_3/Alg$ and Pb(II) to form an electrostatic repulsion between them, thus inhibiting the adsorption capacity. When the initial pH was in the range of 4–7, the pH values after adsorption were all stable at approximately 6, and there was no significant difference in adsorption amount. This may be due to the residual $CaCO_3$ within the $MoS_2B/CaCO_3/Alg$ gel beads, which acted as a pH buffer. As the pH of the solution gradually increased, ion competition and protonation diminished and chelation and ion exchange were enhanced, resulting in a significant increase in adsorption [32]. A pH of 4 was chosen for subsequent tests because lead-containing wastewater is generally acidic in practical applications.

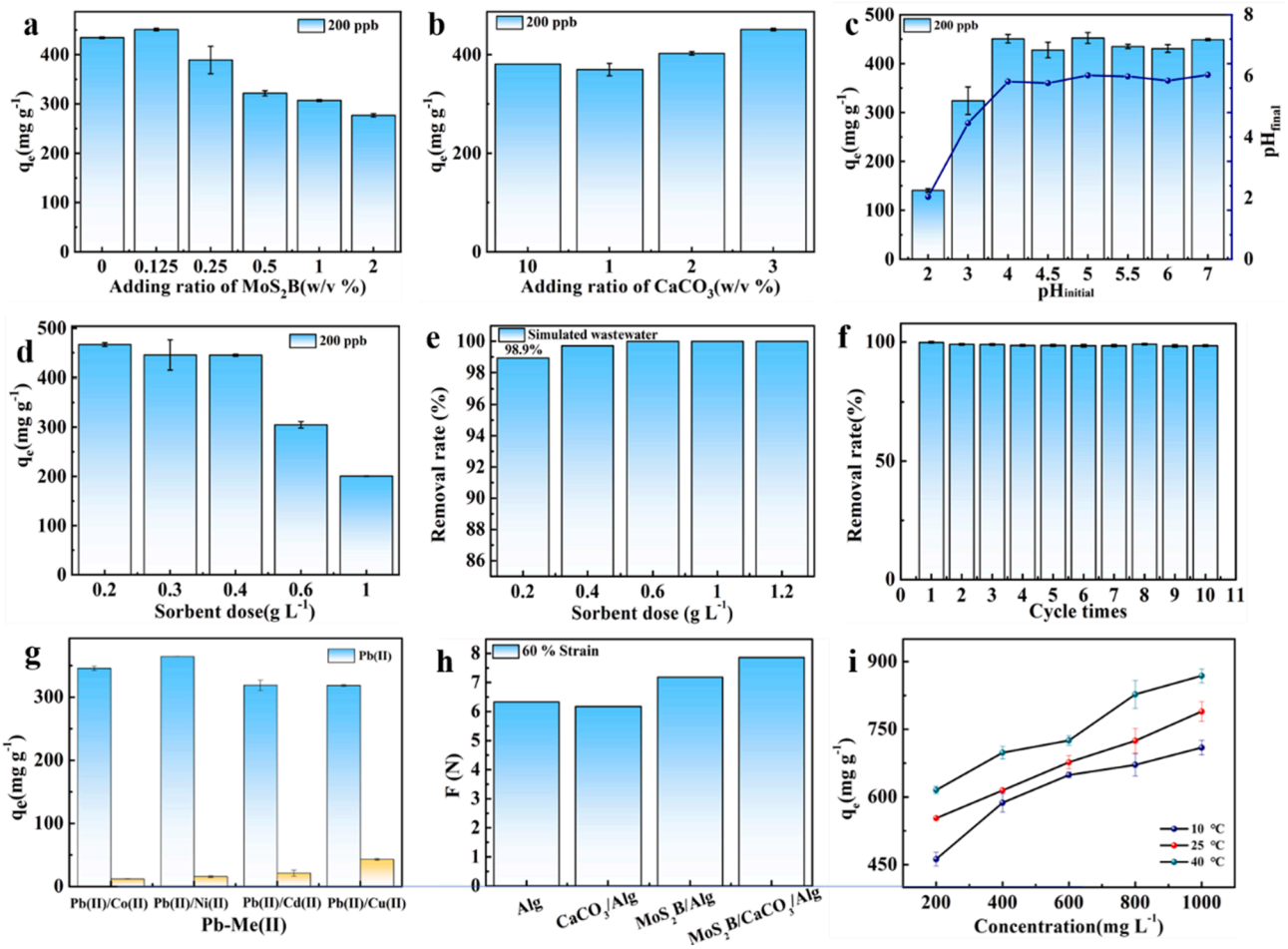

Fig. 3. Effects of different MoS_2B and $CaCO_3$ addition ratios on adsorption **(a, b)**, effect of pH on $MoS_2B/CaCO_3$/Alg adsorption **(c)**, effects of $MoS_2B/CaCO_3$/Alg dosage on adsorption and treatment of simulated battery wastewater **(d, e)**, effect of $MoS_2B/CaCO_3$/Alg cycle times on Pb(II) removal rate **(f)**, influence of coexisting ions on Pb(II) adsorption in binary system**(g)**, comparison of mechanical properties of different materials **(h)**, adsorption capacity of $MoS_2B/CaCO_3$/Alg at different temperatures **(i)**.

As the temperature increased, the Brownian motion of Pb(II) in the solution increased. Therefore, Pb(II) in the solution accelerated into the interior of the gel beads, and for alginate gel beads with 3D microporous and mesoporous structures (Fig. 2**i**), the internal pores were large enough to allow Pb(II) to enter the internal adsorption sites. The actual maximum adsorption volumes at 10, 25, and 40 °C were 709.4, 799.1, and 868.6 mg g^{-1}, respectively. Therefore, the heat consumption during Pb(II) adsorption by $MoS_2B/CaCO_3$/Alg, with $\Delta H_0 > 0$, also implies that the adsorption process is heat-absorbing (Table 1). The small ΔH_0 value also suggests that physical interaction is a part of the mechanism of the adsorption process, and this is further supported by the adsorption isotherm and kinetic results. The adsorption of Pb(II) by $MoS_2B/CaCO_3$/Alg shows a negative increase in ΔG_0 at 10–40 °C, proving that it is a spontaneous reaction and that positively affects adsorption. In addition, the entropy change (ΔS_0) value was positive, indicating that $MoS_2B/CaCO_3$/Alg has a high affinity for Pb(II) and that the disorder at the solid–liquid interface increases during adsorption [33].

Table 1
Thermodynamic parameters of $MoS_2B/CaCO_3$/Alg on Pb(II).

Temperature(°C)	ΔG^o kJ mol^{-1}	ΔH^o kJ mol^{-1}	$\Delta S^o k$ J K^{-1} mol^{-1}
10	–18.67	6.65	0.09
25	–19.70		
40	–21.22		

3.4. Adsorption kinetic

The adsorption curves for both high and low concentrations increased rapidly in the first 2 h, reaching approximately 50 % at 6 h (Fig. 4**a**). After 12 h, the adsorption began to level off, reaching 80 % at 24 h (464 mg g^{-1} and 661 mg g^{-1}) and 566 mg g^{-1} and 725 mg g^{-1} after 72 h. Therefore, to save time and cost, subsequent experiments were carried out with an adsorption time of 24 h.

After fitting pseudo-first-order (PFO) and pseudo-second-order (PSO) kinetic models (Table 2), the correlation coefficients for PSO (0.999 and 0.975) were higher than those for PSO (0.991 and 0.949). This indicates that the adsorption of Pb(II) by porous $MoS_2B/CaCO_3$/Alg gel bead is mainly controlled by chemisorption [34].

Based on the intraparticle diffusion model, the adsorption profile (Fig. 4**b**) was divided into three linear parts with diffusion rate constants $K_1 > K_2 > K_3$, none of which passed the origin, indicating that the outer surface adsorption, transition phase, and final equilibrium phase were included. The outer surface adsorption phase took approximately 120 mins, the film diffusion phase took 600 mins, and then entered the intraparticle diffusion step [35]. According to the Boyd model fit (Fig. 4**c**), the fitted line did not pass the origin, and the D_i values were 1.11×10^{-6} and 8.11×10^{-7} for low and high concentrations, respectively (Table 3), indicating that the adsorption rate of Pb(II) by $MoS_2B/CaCO_3$/Alg was mainly controlled by liquid film diffusion [36].

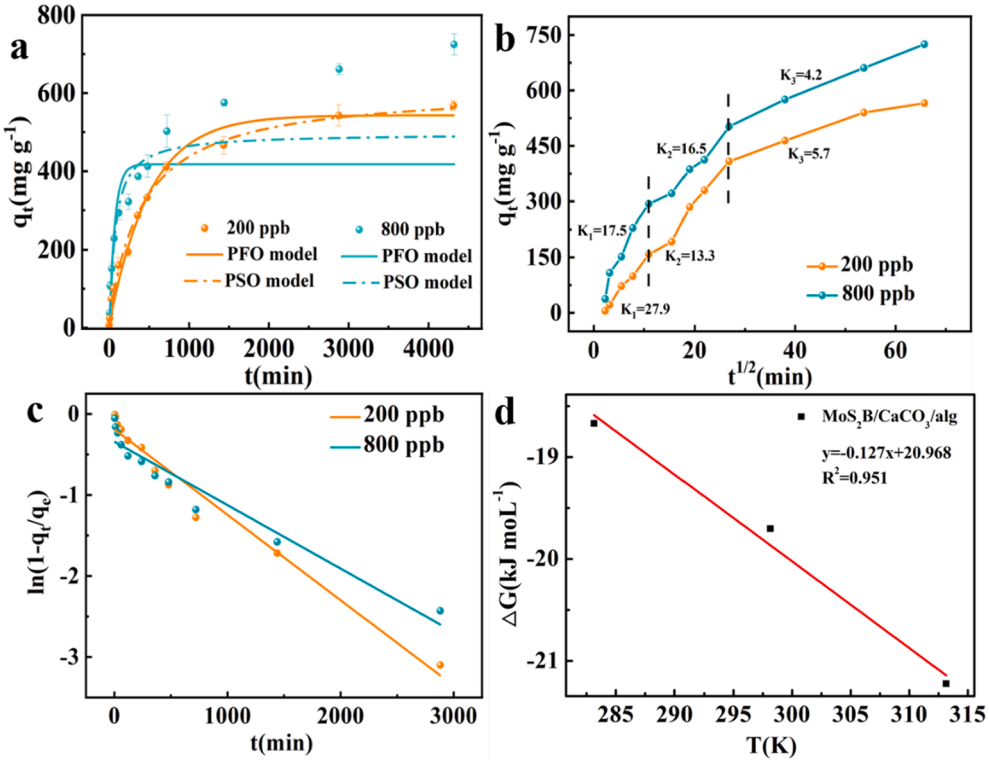

Fig. 4. Change in the adsorption capacity of $MoS_2B/CaCO_3$/Alg with time and adsorption kinetics modeled with the PFO equation and PSO equation **(a)**, intra-particle diffusion model for Pb(II) adsorption on $MoS_2B/CaCO_3$/Alg **(b)**, Boyd model of $MoS_2B/CaCO_3$/Alg **(c)**, thermodynamic fitting curve of $MoS_2B/CaCO_3$/Alg **(d)**.

Table 2
PFO and PSO model parameters.

	Pseudo-first order				Pseudo-second order	
Pb(II) concentration	q_e	K_1	R^2	q_e	K_2	R^2
ppb	mg g^{-1}	min^{-1}		m^{-1}	g m^{-1} min^{-1}	
200	540.8	0.002	0.991	613.1	4.0×10^{-6}	0.999
800	417.5	0.014	0.949	714.3	2.9×10^{-5}	0.975

3.5. Adsorption isotherms and comparative studies

Temperature is an important factor affecting the adsorption of Pb(II) by adsorbents, therefore, the Langmuir, Freundlich and Temkin isotherm models were used to fit the effect of $MoS_2B/CaCO_3$/Alg on the adsorption of Pb(II) at 10, 25, and 40 °C. The relevant parameters are listed in Table 5. $MoS_2B/CaCO_3$/Alg in the adsorption of Pb(II) correlated well with both the Langmuir and Freundlich models, and both models were suitable for fitting the experimental data, indicating that the adsorption of Pb(II) by $MoS_2B/CaCO_3$/Alg is a complex process rather than a simple monolayer or multilayer adsorption. The adsorption of $MoS_2B/CaCO_3$/Alg increased with increasing with temperature, and the maximum adsorption capacities obtained using the Langmuir model were 769.2, 833.3, and 909.1 mg g^{-1} at 10, 25, and 40 °C, respectively (Table 5). $MoS_2B/CaCO_3$/Alg showed excellent removal capacity Pb(II) compared to similar alginate gel adsorbent materials (Table 4).

In the Freundlich model, the empirical constants 1/n calculated for the high K_F values obtained were all less than 0.2, indicating ease of adsorption and that the adsorption process was mainly chemisorption. The Temkin model also indicated strong intermolecular forces between Pb(II) and $MoS_2B/CaCO_3$/Alg during Pb(II) adsorption. When $b_T < -40$ kJ mol^{-1}, this indicates that the adsorption process was typical of physical adsorption; when $8 < b_T$ less than 16 kJ mol^{-1}, this indicates that the adsorption process was associated with ion exchange. In the present study, the small values of b_T (0.051–0.074 kJ mol^{-1}) suggest that $MoS_2B/CaCO_3$/Alg may involve both physical and chemisorption in the adsorption process.

3.6. Effect of coexisting ions on the adsorption capacity of $MoS_2B/CaCO_3$/Alg

Divalent metal cations coexisting with Pb(II) are usually present in wastewater, competing with Pb(II) for active sites in the adsorbent. Therefore, the effects of several common toxic divalent heavy metal cations (Co(II), Ni(II), Cd(II), and Cu(II)) on the adsorption of Pb(II) on the $MoS_2B/CaCO_3$/Alg beads were evaluated. Fig. 3**g** shows the adsorption behavior of $MoS_2B/CaCO_3$/Alg in the Pb(II)-Me(II) binary

Table 3
Parameters of the intra-particle diffusion model and Boyd model.

	Intra-particle diffusion model						Boyd model	
Pb(II)	K_1	R_1^2	K_2	R_2^2	K_3	R_3^2	D	R^2
ppb	mg g^{-1} $min^{-1/2}$		mg g^{-1} $min^{-1/2}$		mg g^{-1} $min^{-1/2}$		cm^2 s^{-1}	
200	17.5	0.983	16.5	0.976	2.3	0.975	1.11×10^{-6}	0.972
800	27.9	0.967	11.9	0.959	2.0	0.932	8.11×10^{-7}	0.943

Table 4
Comparison of adsorption capacities of adsorbents for the removal of Pb(II).

Adsorbent	pH	Adsorption Capacity mg g^{-1}	Reference
Fe_3S_4/Alg-Ca beads	6	126.4	[37]
3D-MMTNs hydrogel	5	134	[38]
SH-SiO_2 MS-Ca-Alg beads	5–7	127.9	[39]
Fe-SA-C	6	796.27	[40]
PEI/ GO-Alg beads	7	602	[41]
CHT/Alg/Fe_3O_4@SiO_2	4.2	234.77	[14]
CPAN-2 membrane	5.5	254.5	[42]
$CM_{0.5}AP_{0.75}$ beads	5	596.68	[43]
SH-Graphene bio-sponge	5	101.01	[44]
Alg_{Ox}–TSC beads	3	950	[45]
Pb-IIP-1 beads	5.5	947.2	[46]
$MoS_2B/CaCO_3$/Alg beads	4	833.3	This work

MMNTS: montmorillonite nanosheets, SH-SiO_2 MS-Ca-Alg: thiol functionalized silica microspheres loaded alginate, Fe-SA-C: biochar-interpenetrated iron-alginate hydrogel, PEI/ GO: PEI-modified graphene oxide, CHT: chitosan, CPAN-2: CaAlg/PAN-UiO-66-$(COOH)_2$, $CM_{0.5}AP_{0.75}$: polyethyleneimine/melamine co-functionalized alginate, Pb-IIP-1: PEI modified ion imprinted SA beads, Alg_{Ox}–TSC: Thiosemicarbazide modified alginate.

system. Co(II) and Ni(II) had only a slight effect, whereas Cd(II) and Cu (II) had no strong effect on the adsorption of Pb(II). The amount of Pb(II) adsorbed in the Pb(II)/M(II) system was not significantly different from that of the single Pb(II) system (408 mg g^{-1}),which were 345.7 mg g^{-1} for Pb(II)/Co(II), 364.3 mg g^{-1} for Pb(II)/Ni(II), 319.1 mg g^{-1} for Pb (II)/Cd(II), 318.6 mg g^{-1} for Pb(II)/Cu(II). In general, the effect of Pb(II) adsorption followed the order Cu(II) > Cd(II) > Co(II) > Ni(II) (Table 6). This difference may be due to the different electronegativities of the metal ions (2.3 for Pb(II), 1.90 for Cu(II), 1.88 for Co(II), 1.69 for Cd(II), 1.91 for Ni(II)) and the mass-to-nucleus ratio (Pb(II) is 103, Cu(II) is 32, Co(II) is 29, Cd(II) is 56, Ni(II) is 29). The high affinity for Cu(II) may be attributed to the Jahn-Teller effect [45].

3.7. Removal of Pb(II) from simulated lead battery wastewater

The ability of $MoS_2B/CaCO_3$/Alg to remove Pb(II) from real wastewater was evaluated after adjusting the pH of the simulated wastewater to 4 according to Wang et al. [46] in a laboratory simulated lead battery wastewater with the same composition and concentration. By varying the dosage of $MoS_2B/CaCO_3$/Alg, it was found that 98.9 % of Pb(II) could be removed from the wastewater at a dosage of only 0.2 g L^{-1}, and at a dosage of 0.4 g L^{-1}, the Pb(II) concentration in the wastewater could be reduced to 0.0092 ppm, which is much lower than the current Chinese emission standard for pollutants in the battery industry (GB 30484–2013) This indicates that $MoS_2B/CaCO_3$/Alg is highly resistant to interference and has a wide potential for practical application.

3.8. Desorption experiments

Testing the regeneration performance of the adsorbent is essential for assessing its stability and potential for large-scale applications of $MoS_2B/CaCO_3$/Alg. The removal of Pb(II) by $MoS_2B/CaCO_3$/Alg showed only a slight decrease of approximately 0.8 % after the first cycle, and remained at 98.4 % after 10 cycles, demonstrating its excellent recyclability. At the same time $MoS_2B/CaCO_3$/Alg maintained an intact gel bead morphology after 10 consecutive cycles, without cracking, proving its solid mechanical properties, and supporting its scope for practical application (**Fig.S6** Comparative photos of adsorbent before and after ten cycles).

3.9. Possible pathways for Pb(II) removal by $MoS_2B/CaCO_3$/Alg

The adsorption mechanism of $MoS_2B/CaCO_3$/Alg on Pb(II) was analyzed by EDS, FTIR and XPS. The residual $CaCO_3$ in $MoS_2B/CaCO_3$/Alg (**Fig.S1 and S2**) was uniformly distributed in the gel beads and the proportion of Ca(II) decreased from 8.21 % to 2.25 % by weight after adsorption, demonstrating that $CaCO_3$ and Ca(II) in the alginate skeleton were involved in the adsorption process via ion exchange with Pb (II). Residual $CaCO_3$ can act as a pH buffer component of the solution (Fig. 3**c**), facilitating the effective adsorption of Pb(II) by the adsorbent over a wide pH range. $CaCO_3$ can also provide additional adsorption active sites for Pb(II) to be removed by exchange with Ca(II) ions by forming $PbCO_3$ surface precipitates [20]. However, $CaCO_3$ was not a major contributor to the adsorption of Pb(II) by $MoS_2B/CaCO_3$/Alg, due to its relatively small proportion in the gel beads.

Furthermore, the FTIR spectra before and after the adsorption indicated that the O-containing groups changed before and after the adsorption. O—H shifted back from 3347 cm^{-1} to 3328 cm^{-1}, and the asymmetric and symmetric peaks of COO– shifted from 1609 cm^{-1} to 1589 cm^{-1} and 1426 cm^{-1} to 1414 cm^{-1}, respectively, along with the weakened intensity. This could be because the O-containing groups and the total XPS profile of $MoS_2B/CaCO_3$/Alg-Pb showed for Pb $4d_{3/2}$, Pb $4d_{5/2}$ and Pb 4f, demonstrating that Pb(II) was adsorbed on the adsorbent. The peak at the binding energy of 138.71 eV for Pb $4f_{7/2}$ was presumed to contain 35.6 % of $PbCO_3$. The peaks for Pb $4f_{5/2}$ at 143.59 eV and Pb $4f_{7/2}$ at 137.62 eV presumably contain 47.6 % of Pb—O present, which may be due to the formation of chelates from Pb(II) with carboxyl groups [47], and the XRD and FTIR results are also consistent. Based on the above analysis, it can be speculated that the mechanism of Pb(II) adsorption by $MoS_2B/CaCO_3$/Alg is as follows: (1) At pH 4, $MoS_2B/CaCO_3$/Alg was negatively charged (**Fig. S7**), which was attracted to the positive and negative charges of Pb(II), causing the rapid adsorption of Pb(II) onto the gel beads. (2) COO– and –OH in $MoS_2B/CaCO_3$/Alg chelated with Pb(II). (3) The residual $CaCO_3$ in $MoS_2B/CaCO_3$/Alg and Ca(II) in the alginate skeleton underwent ion exchange with Pb(II).

$$Pb^{2+} + R - COOH \rightarrow R + COOPb^{+} \quad (2)$$

$$Pb^{2+} + 2O - H \rightarrow (O-)_2 Pb + 2H^{+} \quad (3)$$

Table 6
Selective adsorption parameters of $MoS_2B/CaCO_3$/Alg.

Metal ions	K_d (Pb(II), L g^{-1})	K_d (M(II), L g^{-1})	k
Pb(II)/Co(II)	15.76	0.12	137.02
Pb(II)/Ni(II)	16.99	0.16	106.88
Pb(II)/Cd(II)	10.88	0.22	50.48
Pb(II)/Cu(II)	10.60	0.44	24.01

Table 5
Adsorption isotherm parameters of $MoS_2B/CaCO_3$/Alg.

	Langmuir			Freundlich			Temkin		
T	q_{max}	K_L	R^2	K_F	1/n	R^2	K_T	b_T	R^2
°C	mg g^{-1}	L m^{-1}		L m^{-1}			L $^{-1}$	kJ mol^{-1}	
10	769.2	0.013	0.998	192.8	0.195	0.989	0.672	0.074	0.996
25	833.3	0.014	0.987	297.7	0.137	0.908	5.09	0.092	0.875
40	909.1	0.017	0.987	332.7	0.137	0.894	5.16	0.051	0.865

$$Pb^{2+} + CO_3^{2-} \rightarrow PbCO_3 \quad (4)$$

4. Conclusions

In this study, composite gel beads of separable core–shell structured alginate coated with MoS_2B modified biochar and $CaCO_3$ were prepared for the removal of Pb(II) from water using a simple method, based on the synergistic effect between the materials to enhance adsorption. MoS_2B/$CaCO_3$/Alg showed good removal over a wide pH range of pH 4–7, which was attributed to the residual $CaCO_3$ in the adsorbent acting as a pH buffer. $CaCO_3$ was also found to have an enhanced effect on Pb(II) adsorption. The removal mechanism of Pb(II) by MoS_2B/$CaCO_3$/Alg is primarily ion exchange, and electrostatic attraction. The maximum adsorption capacities obtained for the MoS_2B/$CaCO_3$/Alg gel beads at pH 4 using the Langmuir model were 769.2, 833.3, and 909.1 mg g^{-1} at 10, 25, and 40 °C, respectively. MoS_2B/$CaCO_3$/Alg also exhibited excellent interference resistance and reusability. In conclusion, MoS_2B/$CaCO_3$/Alg is a promising adsorbent because it is simple to prepare, can be produced on a large scale, can be easily separated from water, and can be used to treat specific industrial wastewater.

CRediT authorship contribution statement

Yingnan He: Investigation, Formal analysis, Writing – original draft. **Xiuxiu Jia:** Investigation, Data curation. **Shuxing Zhou:** Resources, Investigation, Writing – review & editing. **Jianbing Chen:** Investigation, Software. **Shusheng Zhang:** Investigation. **Xiaohua Li:** Validation, Methodology. **Yimin Huang:** Supervision, Investigation, Project administration, Writing – review & editing. **Thomas Wågberg:** Validation, Formal analysis. **Guangzhi Hu:** Conceptualization, Funding acquisition, Writing – review & editing.

Declaration of Competing Interest

The authors declare that they have no known competing financial interests or personal relationships that could have appeared to influence the work reported in this paper.

Acknowledgments

This work was supported by the National Key R&D Program of China (2019YFC1804400), Special Project for Social Development of Yunnan Province (202103AC100001), Key Discipline of Materials Science and Engineering of Chizhou University (CZxyylxk03), Anhui Province materials and chemical industry first-class undergraduate talents demonstration leading base (2020rcsfjd28), and Double-First Class University Plan (C176220100042). The authors thank the Advanced Analysis and Measurement Center of Yunnan University for the sample testing service.

Appendix A. Supplementary material

Supplementary data to this article can be found online at https://doi.org/10.1016/j.seppur.2022.122212.

References

[1] H. Qiu, W. Ni, L. Yang, Q. Zhang, Remarkable ability of Pb(II) capture from water by self-assembled metal-phenolic networks prepared with tannic acid and ferric ions, Chem. Eng. J. 450 (2022), 138161.
[2] Z. Chen, X. Huo, G. Chen, X. Luo, X. Xu, Lead (Pb) exposure and heart failure risk, Environ. Sci. Pollut. Res. 28 (2021) 28833–28847.
[3] Y. Liu, L. Hu, Y. Yao, Z. Su, S. Hu, Construction of composite chitosan-glucose hydrogel for adsorption of Co^{2+} ions, Int. J. Biol. Macromol. 139 (2019) 213–220.
[4] R. Dhakal, K. Ghimire, K. Inoue, M. Yano, K. Makino, Acidic polysaccharide gels for selective adsorption of lead (II) ion, Sep. Purif. Technol. 42 (2005) 219–225.
[5] Y. Huang, B. Wang, J. Lv, Y. He, H. Zhang, W. Li, Y. Li, T. Wågberg, G. Hu, Facile synthesis of sodium lignosulfonate/polyethyleneimine/sodium alginate beads with ultra-high adsorption capacity for Cr(VI) removal from water, J. Hazard. Mater. 436 (2022), 129270.
[6] M. Badsha, M. Khan, B. Wu, A. Kumar, I. Lo, Role of surface functional groups of hydrogels in metal adsorption: from performance to mechanism, J. Hazard. Mater. 408 (2021), 124463.
[7] S. Li, Y. Song, H. Yang, Q. An, Z. Xiao, S. Zhai, Modifying alginate beads using polycarboxyl component for enhanced metal ions removal, Int. J. Biol. Macromol. 158 (2020) 493–501.
[8] Q. Feng, M. Chen, P. Wu, X. Zhang, S. Wang, Z. Yu, B. Wang, Simultaneous reclaiming phosphate and ammonium from aqueous solutions by calcium alginate-biochar composite: sorption performance and governing mechanisms, Chem. Eng. J. 429 (2022), 132166.
[9] B. Wang, Y. Wan, Y. Zheng, X. Lee, T. Liu, Z. Yu, J. Huang, Y.S. Ok, J. Chen, B. Gao, Alginate-based composites for environmental applications: a critical review, Critical Rev. Environ. Sci. Technol. 49 (2019) 318–356.
[10] W. Zhang, J. Ou, M. Tang, Q. He, A. Long, S. Luo, S. Sun, J. Wan, Y. Gao, L. Zhou, B. Wang, H. Wang, Physically-crosslinked activated $CaCO_3$/polyaniline-polypyrrole-modified GO/alginate hydrogel sorbent with highly efficient removal of copper(II) from aqueous solution, Chem. Eng. J. 431 (2022), 133375.
[11] X. Cui, X. Dai, K. Khan, T. Li, X. Yang, Z. He, Removal of phosphate from aqueous solution using magnesium-alginate/chitosan modified biochar microspheres derived from Thalia dealbata, Bioresour. Technol. 218 (2016) 1123–1132.
[12] C. Lei, Y. Song, F. Meng, Y. Sun, D.C.W. Tsang, K. Yang, D. Lin, Iron-crosslinked alginate derived Fe/C composites for atrazine removal from water, Sci. Total Environ. 756 (2021), 143866.
[13] Z. Lin, Y. Yang, Z. Liang, L. Zeng, A. Zhang, Preparation of chitosan/calcium alginate/bentonite composite hydrogel and its heavy metal ions adsorption properties, Polymers 13 (2021).
[14] D. Facchi, A. Cazetta, E. Canesin, V. Almeida, E. Bonafé, M. Kipper, A. Martins, New magnetic chitosan/alginate/Fe_3O_4@SiO_2 hydrogel composites applied for removal of Pb(II) ions from aqueous systems, Chem. Eng. J. 337 (2018) 595–608.
[15] Z. Khan, M. Gao, J. Wu, R. Bi, C.T. Mehmood, Z. Song, Mechanism of As(III) removal properties of biochar-supported molybdenum-disulfide/iron-oxide system, Environ. Pollut. 287 (2021), 117600.
[16] N. Luo, C. Chen, D. Yang, W. Hu, F. Dong, S defect-rich ultrathin 2D MoS_2: The role of S point-defects and S stripping-defects in the removal of Cr(VI) via synergistic adsorption and photocatalysis, Appl. Catal. B: Environ. 299 (2021), 120664.
[17] Z. Khan, M. Gao, W. Qiu, Z. Song, Properties and adsorption mechanism of magnetic biochar modified with molybdenum disulfide for cadmium in aqueous solution, Chemosphere 255 (2020), 126995.
[18] L. Ling, W. Liu, S. Zhang, H. Jiang, Magnesium Oxide Embedded Nitrogen Self-Doped Biochar Composites: fast and high-efficiency adsorption of heavy metals in an aqueous solution, Environ. Sci. Technol. 51 (2017) 10081–10089.
[19] H. Zhu, X. Tan, L. Tan, C. Chen, N. Alharbi, T. Hayat, M. Fang, X. Wang, Biochar derived from sawdust embedded with molybdenum disulfide for highly selective removal of Pb^{2+}, ACS Applied Nano Materials 1 (2018) 2689–2698.
[20] P. Wang, T. Shen, X. Li, Y. Tang, Y. Li, Magnetic Mesoporous Calcium Carbonate-Based Nanocomposites for the removal of Toxic Pb(II) and Cd(II) Ions from Water, ACS Applied Nano Materials 3 (2020) 1272–1281.
[21] X. Zhou, W. Liu, J. Zhang, C. Wu, X. Ou, C. Tian, Z. Lin, Z. Dang, Biogenic calcium carbonate with hierarchical organic-inorganic composite structure enhancing the removal of Pb(II) from wastewater, ACS Appl. Mater. Interfaces 9 (2017) 35785–35793.
[22] Q. Zeng, Y. Huang, L. Huang, L. Hu, W. Sun, H. Zhong, Z. He, High adsorption capacity and super selectivity for Pb(II) by a novel adsorbent: Nano humboldtine/almandine composite prepared from natural almandine, Chemosphere 253 (2020), 126650.
[23] H. Zheng, Y. Gao, K. Zhu, Q. Wang, M. Wakeel, A. Wahid, N.S. Alharbi, C. Chen, Investigation of the adsorption mechanisms of Pb(II) and 1-naphthol by β-cyclodextrin modified graphene oxide nanosheets from aqueous solution, J. Colloid Interface Sci. 530 (2018) 154–162.
[24] F. Lyu, S. Niu, L. Wang, R. Liu, W. Sun, D. He, Efficient removal of Pb(II) ions from aqueous solution by modified red mud, J. Hazard. Mater. 406 (2021), 124678.
[25] L. Kong, Z. Li, X. Huang, S. Huang, H. Sun, M. Liu, L. Li, Efficient removal of Pb(II) from water using magnetic Fe_3S_4/reduced graphene oxide composites, J. Mater. Chem. A 5 (2017) 19333–19342.
[26] S. Wang, S. Bian, J. Liu, J. Li, S. Xu, Z. Liang, Highly adsorptive pristine and magnetic biochars prepared from crayfish shell for removal of Cu(II) and Pb(II), J. Taiwan Inst. Chem. Eng. 127 (2021) 175–185.
[27] X. Wang, Y. Ye, X. Wu, J.R. Smyth, Y. Yang, Z. Zhang, Z. Wang, High-temperature Raman and FTIR study of aragonite-group carbonates, Phys. Chem. Miner. 46 (2019) 51–62.
[28] A. Pourjavadi, M. Nazari, B. Kabiri, S. Hosseini, C. Bennett, Preparation of porous graphene oxide/hydrogel nanocomposites and their ability for efficient adsorption of methylene blue, RSC Adv. 6 (2016) 10430–10437.
[29] C. Johnson, G. Furrer, Influence of Biodegradation Processes on the Duration of $CaCO_3$ as a pH Buffer in Municipal Solid Waste Incinerator Bottom Ash, Environ. Sci. Technol. 36 (2002) 215–220.
[30] M. Islam, W. Choi, B. Nam, C. Yoon, H. Lee, Needle-like iron oxide@$CaCO_3$ adsorbents for ultrafast removal of anionic and cationic heavy metal ions, Chem. Eng. J. 307 (2017) 208–219.
[31] H. Ge, J. Du, Selective adsorption of Pb(II) and Hg(II) on melamine-grafted chitosan, Int. J. Biol. Macromol. 162 (2020) 1880–1887.
[32] C. Fan, K. Li, J. Li, D. Ying, Y. Wang, J. Jia, Comparative and competitive adsorption of Pb(II) and Cu(II) using tetraethylenepentamine modified chitosan/$CoFe_2O_4$ particles, J. Hazard. Mater. 326 (2017) 211–220.

[33] P. Gu, J. Xing, T. Wen, R. Zhang, J. Wang, G. Zhao, T. Hayat, Y. Ai, Z. Lin, X. Wang, Experimental and theoretical calculation investigation on efficient Pb(II) adsorption on etched Ti_3AlC_2 nanofibers and nanosheets, Environ. Sci. NANO 5 (2018) 946–955.
[34] J. Zhao, C. Wang, S. Wang, Y. Zhou, Experimental and DFT study of selective adsorption mechanisms of Pb(II) by UiO-66-NH_2 modified with 1,8-dihydroxyanthraquinone, J. Ind. Eng. Chem. 83 (2020) 111–122.
[35] M. Kapur, M. Mondal, Mass transfer and related phenomena for Cr(VI) adsorption from aqueous solutions onto Mangifera indica sawdust, Chem. Eng. J. 218 (2013) 138–146.
[36] A. Öztürk, E. Malkoc, Adsorptive potential of cationic Basic Yellow 2 (BY_2) dye onto natural untreated clay (NUC) from aqueous phase: mass transfer analysis, kinetic and equilibrium profile, Appl. Surf. Sci. 299 (2014) 105–115.
[37] L. Lan, B. Liu, W. Li, H. Bu, T. Hu, H. Hu, Y. Li, G. Jiang, Facilely recoverable Pb(II) adsorbent based on greigite (Fe_3S_4) loaded alginate aerogel with high adsorption efficiency, Chemosphere 290 (2022), 133264.
[38] Y. Miao, W. Peng, W. Wang, Y. Cao, H. Li, L. Chang, Y. Huang, G. Fan, H. Yi, Y. Zhao, T. Zhang, 3D-printed montmorillonite nanosheets based hydrogel with biocompatible polymers as excellent adsorbent for Pb(II) removal, Sep. Purif. Technol. 283 (2022), 120176.
[39] S. Singh, H. Basu, M. Bassan, R. Singhal, Thiol functionalised silica microsphere loaded polymeric hydrogel: development of a novel hybrid sorbent for removal of lead and cadmium, Chemosphere 286 (2022), 131659.
[40] C. Zhao, L. Hu, C. Zhang, S. Wang, X. Wang, Z. Huo, Preparation of biochar-interpenetrated iron-alginate hydrogel as a pH-independent sorbent for removal of Cr(VI) and Pb(II), Environ. Pollut. 287 (2021), 117303.
[41] F. Arshad, M. Selvaraj, J. Zain, F. Banat, M.A. Haija, Polyethylenimine modified graphene oxide hydrogel composite as an efficient adsorbent for heavy metal ions, Sep. Purif. Technol. 209 (2019) 870–880.
[42] T. Zhang, P. Li, S. Ding, X. Wang, High-performance TFNC membrane with adsorption assisted for removal of Pb(II) and other contaminants, J. Hazard. Mater. 424 (2022), 127742.
[43] S. Bo, J. Luo, Q. An, Z. Xiao, H. Wang, W. Cai, S. Zhai, Z. Li, Efficiently selective adsorption of Pb(II) with functionalized alginate-based adsorbent in batch/column systems: mechanism and application simulation, J. Cleaner Prod. 250 (2020), 119585.
[44] P. Yap, Y. Auyoong, K. Hassan, F. Farivar, D. Tran, J. Ma, D. Losic, Multithiol functionalized graphene bio-sponge via photoinitiated thiol-ene click chemistry for efficient heavy metal ions adsorption, Chem. Eng. J. 395 (2020), 124965.
[45] H. Yu, Y. Dai, L. Zhou, J. Ouyang, X. Tang, Z. Liu, A.A. Adesina, Selective biosorption of U(VI) from aqueous solution by ion-imprinted honeycomb-like chitosan/kaolin clay composite foams, Int. J. Biol. Macromol. 206 (2022) 409–421.
[46] Z. Wang, J. Zhang, T. Wen, X. Liu, Y. Wang, H. Yang, J. Sun, J. Feng, S. Dong, J. Sun, Highly effective remediation of Pb(II) and Hg(II) contaminated wastewater and soil by flower-like magnetic MoS_2 nanohybrid, Sci. Total Environ. 699 (2020), 134341.
[47] Y. Cao, W. Xiao, G. Shen, G. Ji, Y. Zhang, C. Gao, L. Han, Carbonization and ball milling on the enhancement of Pb(II) adsorption by wheat straw: competitive effects of ion exchange and precipitation, Bioresour. Technol. 273 (2019) 70–76.